

Chapter 8

Numerical Techniques

The rod, beam, plate and shell models developed in Chapter 7 generally preclude analytic solution due to the boundary conditions and piecewise nature of material parameters and exogenous inputs. This necessitates the development of approximation techniques appropriate not only for simulations and transducer characterization but also for optimization and control design. Whereas we focus primarily on the first objective in this chapter, the use of these numerical models for subsequent transducer optimization and control design dictates that attention be paid to additional criteria, such as adjoint convergence, that arise in the context of constrained optimization — the reader is referred to [67] and references therein for details regarding approximation techniques pertaining to optimization and control formulations.

For all of the models, we first employ Galerkin approximations in space to obtain semi-discrete, vector-valued ODE that evolve in time — see pages 417–419 of Appendix A for a general discussion regarding the relation between Galerkin and finite element methods. This provides a natural setting for linear and nonlinear finite-dimensional control design and direct simulations. Since Galerkin or finite element approximation in space typically yield moderately stiff ODE systems, A-stable or stiff algorithms are advised when approximating solutions in time; this includes trapezoidal-based approximations or routines such as `ode15s.m` in MATLAB.

In all cases, we consider approximation in the context of the weak model formulations since this reduces smoothness requirements and accommodates in a natural manner discontinuous material parameters and inputs. This necessarily involves the integration of polynomial or trigonometric basis elements which we accomplish using Gaussian quadrature routines chosen to ensure exact integration for linear and cubic basis functions. We summarize these numerical integration algorithms in Section 8.1. Approximation techniques for rods, beams, plates and shells are subsequently described in Section 8.2–8.5.

Numerical approximation of distributed structural models is an extremely broad topic and includes issues such as shear locking and approximation techniques for control design which constitute active research areas. Rather than attempt to

provide a comprehensive description of numerical techniques, we instead summarize certain fundamental methods appropriate for smart structures and indicate pitfalls and directions required to extend the algorithms to more complex settings. The reader is referred to [54, 479] for finite element theory, [390, 462, 527] for finite element implementation techniques, and [163, 383, 406] for the theory of splines, variational methods and Galerkin techniques. A detailed discussion illustrating finite element implementation in MATLAB is provided in [276] and m-files for implementing various models discussed in this chapter are provided at the website <http://www.siam.org/books/fr32>. Additional references specific to the various structures will be indicated in relevant sections.

8.1 Quadrature Techniques

Consider integrals of the form $I = \int_a^b f(x)dx$ where (a, b) is either finite or infinite and the value I is finite. The goal in numerical integration or quadrature is to approximate I by finite sums of the form

$$I_n = \sum_{i=0}^n w_i f(x_i)$$

where w_i and x_i respectively denote quadrature weights and nodes. Various approximation theories — e.g., based on Taylor expansions or the theory of orthogonal polynomials — yield choices for w_i and x_i that determine the rate at which I_n converges to I as $n \rightarrow \infty$.

8.1.1 Newton–Cotes Formulae

To illustrate issues associated with the choice of weights and nodes, we consider first closed and open Newton–Cotes formulae for finite $[a, b]$. The nodes for the two cases are $x_i = x_0 + ih$ where $i = 0, \dots, n$ and

$$h = \frac{b-a}{n}, x_0 = a, \text{ closed Newton–Cotes formulae}$$

$$h = \frac{b-a}{n+2}, x_0 = a+h, \text{ open Newton–Cotes formulae.}$$

Hence nodes lie in the closed interval $[a, b]$ in the first case and the open interval (a, b) in the second. In all of the following formulae, ξ is a point in (a, b) and f is assumed sufficiently smooth so that requisite derivatives exist and are continuous. Details regarding the derivation of these relations can be found in [19]. The trapezoid and midpoint rules are illustrated in Figure 8.1.

Closed Newton–Cotes Formulae

1. ($n = 1$) Trapezoidal rule

$$\int_a^b f(x)dx = \frac{h}{2}[f(x_0) + f(x_1)] - \frac{h^3}{12}f''(\xi) \tag{8.1}$$

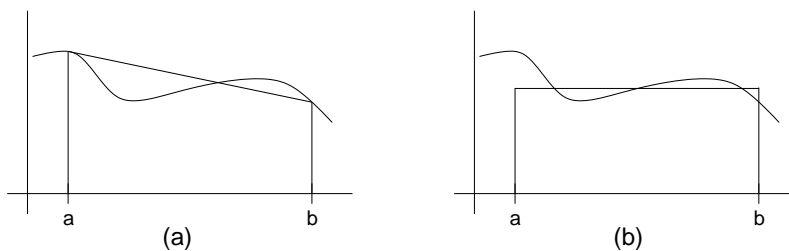


Figure 8.1. (a) Trapezoidal rule and (b) midpoint rule for the interval $[a, b]$.

2. ($n = 2$) Simpson's rule

$$\int_a^b f(x)dx = \frac{h}{3}[f(x_0) + 4f(x_1) + f(x_2)] - \frac{h^5}{90}f^{(4)}(\xi) \quad (8.2)$$

3. ($n = 3$) Simpson's three-eighths rule

$$\int_a^b f(x)dx = \frac{3h}{8}[f(x_0) + 3f(x_1) + 3f(x_2) + f(x_3)] - \frac{3h^5}{80}f^{(4)}(\xi) \quad (8.3)$$

4. ($n = 4$) Milne's rule

$$\int_a^b f(x)dx = \frac{2h}{45}[7f(x_0) + 32f(x_1) + 12f(x_2) + 32f(x_3) + 7f(x_4)] - \frac{8h^7}{945}f^{(6)}(\xi) \quad (8.4)$$

Open Newton-Cotes Formulae

1. ($n = 0$) Midpoint rule

$$\int_a^b f(x)dx = 2hf(x_0) + \frac{h^3}{3}f''(\xi) \quad (8.5)$$

2. ($n = 1$)

$$\int_a^b f(x)dx = \frac{3h}{2}[f(x_0) + f(x_1)] + \frac{3h^3}{4}f''(\xi) \quad (8.6)$$

3. ($n = 2$)

$$\int_a^b f(x)dx = \frac{4h}{3}[2f(x_0) - f(x_1) + 2f(x_2)] + \frac{14h^5}{45}f^{(4)}(\xi) \quad (8.7)$$

4. ($n = 3$)

$$\int_a^b f(x)dx = \frac{5h}{24}[11f(x_0) + f(x_1) + f(x_2) + 11f(x_3)] + \frac{95h^5}{144}f^{(4)}(\xi) \quad (8.8)$$

Accuracy of the Newton–Cotes Formulae

A numerical quadrature formula I_n is said to have *degree of precision* m if $I_n = I$ for all polynomials f such that $\deg(f) \leq m$ and $I_n \neq I$ for $\deg(f) = m + 1$. Hence the trapezoid rule has degree of precision 1 which corroborates the observation that it integrates linear polynomials exactly. It is observed that formulae with an even index gain an extra degree of precision when compared with odd formulae which often makes them preferable. For later comparison with Gaussian quadrature routines, we note that the errors E_n and degrees of precision DP_n for the Newton–Cotes formulae are

$$|E_n| = \begin{cases} K_{1n}h^{n+2}f^{(n+1)}(\xi) & , \quad n \text{ odd} \\ K_{2n}h^{n+3}f^{(n+2)}(\xi) & , \quad n \text{ even} \end{cases}$$

and

$$DP_n = \begin{cases} n & , \quad n \text{ odd} \\ n + 1 & , \quad n \text{ even} \end{cases}$$

where K_{1n} and K_{2n} are constants and it is assumed that $f \in C^{n+2}[a, b]$ if n is even and $f \in C^{n+1}[a, b]$ for odd n .

Whereas increasing n leads to improved accuracy, Newton–Cotes formulae are typically restricted to $n \leq 8$ to avoid stability issues. To achieve the requisite accuracy on large intervals $[a, b]$, including infinite intervals, alternatives are required. These include Romberg integration techniques which improve accuracy through Richardson extrapolation, composite rules, and Gaussian quadrature techniques. We summarize next the latter two options.

Composite Quadrature Techniques

An obvious technique to improve accuracy is to partition finite domains $[a, b]$ into subintervals and then apply the quadrature rules on each subinterval. The manner through which partitions are constructed depends on the choice of open versus closed Newton–Cotes formulae as illustrated in Figure 8.2 for the composite trapezoid and midpoint formulae. In both cases, it is assumed that $f \in C^2[a, b]$ and ξ is a point in (a, b) .

Composite Trapezoidal Rule

The composite trapezoid rule for n subintervals is

$$\int_a^b f(x)dx = \frac{h}{2} \left[f(a) + \sum_{i=1}^{n-1} f(x_i) + f(b) \right] - \frac{b-a}{12} h^2 f''(\xi)$$

where $h = \frac{b-a}{n}$ and $x_i = a + ih$ for $i = 0, \dots, n$. It is observed from Figure 8.2 that if n is doubled, present values of $f(x_i)$ are re-used, thus contributing to the efficiency of the method.

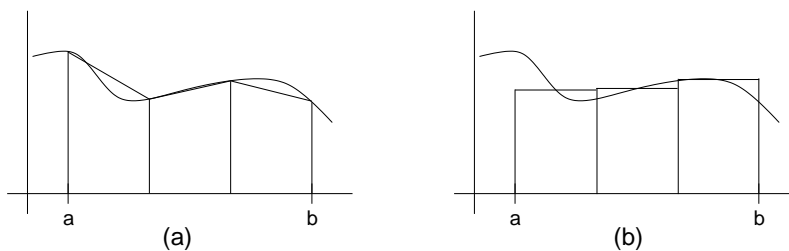


Figure 8.2. (a) Composite trapezoidal rule and (b) composite midpoint rule with three subintervals.

Composite Midpoint Rule

The composite midpoint formula for even n and $\frac{n}{2} + 1$ subintervals is

$$\int_a^b f(x)dx = 2h \sum_{i=0}^{n/2} f(x_i) + \frac{b-a}{6} h^2 f''(\xi).$$

Here $h = \frac{b-a}{n+2}$ and $x_i = a + (2i + 1)h$ for $i = 0, \dots, n$. The approximation obtained with $n = 4$, and hence 3 subintervals is illustrated in Figure 8.2(b).

8.1.2 Gaussian Quadrature Techniques

It is observed that for the open and closed Newton–Cotes formulae, and corresponding composite rules, the quadrature points x_i are fixed *a priori* and quadrature weights w_i are determined to achieve a specified level of accuracy. Hence both the accuracy and degree of precision for the methods are roughly equivalent to the degrees of freedom associated with the weights. Alternatively, one can let both x_i and w_i be free parameters to achieve a maximal order of accuracy. This is the basis for Gaussian quadrature routines which provides the capability for exactly integrating polynomials up to degree $2n - 1$ using n -point expansions.

To provide intuition, we initially consider the expansion

$$\int_{-1}^1 f(x)dx \approx \sum_{i=1}^n f(x_i)w_i$$

with $n = 1$ and $n = 2$. Defining the error as

$$E_n(f) = \int_{-1}^1 f(x)dx - \sum_{i=1}^n f(x_i)w_i,$$

we note that for polynomials $p_m = a_0 + a_1x + \dots + a_mx^m$,

$$E_n(p_m) = a_0E_n(1) + a_1E_n(x) + \dots + a_mE_n(x^m).$$

It thus follows that the integration rule has degree of precision m if

$$E_n(x^i) = 0 \quad , \quad i = 0, \dots, m.$$

1-Point Gaussian Quadrature

To determine the two parameters x_1 and w_1 , we consider the constraints

$$E_1(1) = 0, \quad E_1(x) = 0$$

or

$$\int_{-1}^1 1 dx - w_1 = 0, \quad \int_{-1}^1 x dx - w_1 x_1 = 0.$$

This yields $x_1 = 0$ and $w_1 = 2$ and the general quadrature rule

$$\int_{-1}^1 f(x) dx \approx 2f(0).$$

Note that this is simply the midpoint formula (8.5) which is illustrated for the interval $[a, b]$ in Figure 8.1(b).

2-Point Gaussian Quadrature

Here there are four parameters x_1, x_2, w_1, w_2 and four constraints

$$E_2(x^i) = \int_{-1}^1 x^i dx - (w_1 x_1^i + w_2 x_2^i) = 0, \quad i = 0, 1, 2, 3.$$

This yields the nonlinear system of equations

$$\begin{aligned} w_1 + w_2 &= 2 \\ w_1 x_1 + w_2 x_2 &= 0 \\ w_1 x_1^2 + w_2 x_2^2 &= \frac{2}{3} \\ w_1 x_1^3 + w_2 x_2^3 &= 0 \end{aligned}$$

which has the unique solution

$$\begin{aligned} x_1 &= -\frac{1}{\sqrt{3}}, & w_1 &= 1 \\ x_2 &= \frac{1}{\sqrt{3}}, & w_2 &= 1. \end{aligned}$$

It is noted that the general quadrature rule

$$\int_{-1}^1 f(x) dx \approx f\left(\frac{-1}{\sqrt{3}}\right) + f\left(\frac{1}{\sqrt{3}}\right) \quad (8.9)$$

has the same degree of precision as Simpson's rule (8.2) which required three nodes.

n -Point Gaussian Quadrature

For $n > 2$, solving the nonlinear systems of equations becomes prohibitive and Gaussian quadrature rules are typically formulated using interpolation theory for

orthogonal polynomials. By considering families of orthogonal polynomials defined on the intervals $[-1, 1]$, $[0, \infty)$ and $(-\infty, \infty)$, in addition to weighted integrands, this provides substantial flexibility for approximating a broad range of integrals. A complete discussion of this theory is beyond the scope of this chapter and we refer the reader to [19, 125, 528] for details regarding Gaussian quadrature routines for both single and multivariate approximation.

Gauss–Legendre Quadrature

Gauss–Legendre quadrature formulae are typically defined in terms of degree n Legendre polynomials

$$P_n(x) = \frac{1}{2^n n!} \cdot \frac{d^n}{dx^n} (x^2 - 1)^n, \quad n = 0, 1, 2, \dots$$

on the interval $[-1, 1]$ — see [123, 465] for a derivation of the Legendre polynomials through application of the Gram–Schmidt process to the sequence $1, x, x^2, \dots$. Note that the first five Legendre polynomials are

$$\begin{aligned} P_0(x) &= 1 \\ P_1(x) &= x \\ P_2(x) &= \frac{1}{2}(3x^2 - 1) \\ P_3(x) &= \frac{1}{2}(5x^3 - 3x) \\ P_4(x) &= \frac{1}{8}(35x^4 - 30x^2 + 3). \end{aligned}$$

The quadrature relation is

$$\int_{-1}^1 f(x) dx \approx \sum_{i=1}^n w_i f(x_i) \tag{8.10}$$

where the nodes x_i are zeroes of $P_n(x)$ and the weights are

$$w_i = \frac{-2}{(n + 1)P'_n(x_i)P_{n+1}(x_i)}, \quad i = 1, \dots, n,$$

as summarized in Table 8.1. For $f \in C^{2n}[-1, 1]$, the errors are given by

$$E_n(f) = e_n \frac{f^{(2n)}(\xi)}{(2n)!}$$

where ξ is a point in $[-1, 1]$ and $e_n \approx \frac{\pi}{4^n}$ as $n \rightarrow \infty$ [19]. As noted previously, this implies that the quadrature formula (8.10) is *exact* for polynomials having degree less than or equal to $2n - 1$. Hence when approximating the solution to weak formulations for structural models, the degree n is chosen to be commensurate with finite element or spline basis and test functions.

n	Nodes x_i	Weights w_i
1	0	2
2	$\pm \frac{1}{\sqrt{3}}$	1
3	0 $\pm \sqrt{\frac{3}{5}}$	$\frac{8}{9}$ $\frac{5}{9}$
4	$\pm \frac{\sqrt{15+2\sqrt{30}}}{\sqrt{35}}$ $\pm \frac{\sqrt{15-2\sqrt{30}}}{\sqrt{35}}$	$\frac{49}{6(18+\sqrt{30})}$ $\frac{49}{6(18-\sqrt{30})}$

Table 8.1. Nodes and weights for Gauss–Legendre quadrature on $[-1, 1]$.

Gauss–Laguerre and Gauss–Hermite Quadrature

The integrals in the polarization model (2.114) involve the domains $[0, \infty)$ and $(-\infty, \infty)$. One technique for approximating the integrals is to exploit decay exhibited by the integrand to truncate to finite domains. Alternatively, one can directly approximate the integrals using orthogonal polynomials defined on the half line and real line. This yields the Gauss–Laguerre quadrature relation

$$\int_0^\infty e^{-x} f(x) dx \approx \sum_{i=1}^n w_i f(x_i)$$

and Gauss–Hermite relation

$$\int_{-\infty}^\infty e^{-x^2} f(x) dx \approx \sum_{i=1}^n w_i f(x_i).$$

The weights and nodes for these formulae can be found in [528].

Gauss–Legendre Quadrature on $[a, b]$ and Composite Quadrature

To evaluate integrals on arbitrary domains using the Gauss–Legendre quadrature relation (8.10), one can employ the linear change of variables

$$\int_a^b f(x) dx = \frac{b-a}{2} \int_{-1}^1 f\left(\frac{a+b+\xi(b-a)}{2}\right) d\xi \tag{8.11}$$

to map to the interval $[-1, 1]$. It follows that the nodes and weights x_i and w_i for $[a, b]$ are related to ξ_i and η_i for $[-1, 1]$ by the relations

$$x_i = \frac{a+b}{2} + \frac{b-a}{2} \xi_i \quad , \quad w_i = \frac{b-a}{2} \eta_i.$$

This mapping can also be used to construct composite Gaussian quadrature routines and formulae appropriate for finite element and spline meshes. To illustrate, consider the partition of $[a, b]$ given by $x_j = a + jh$, $h = \frac{b-a}{n}$, for $j = 0, \dots, n$ as illustrated in Figure 8.3. The nodes and weights for the 4-point Gauss–Legendre rule on the subinterval $[x_{j-1}, x_j]$ are then

$$\begin{aligned}
 x_1 &= x_{j-1} + h \left[\frac{1}{2} - \frac{\sqrt{15+2\sqrt{30}}}{2\sqrt{35}} \right], & w_1 &= \frac{49h}{12(18+\sqrt{30})} \\
 x_2 &= x_{j-1} + h \left[\frac{1}{2} - \frac{\sqrt{15-2\sqrt{30}}}{2\sqrt{35}} \right], & w_2 &= \frac{49h}{12(18-\sqrt{30})} \\
 x_3 &= x_{j-1} + h \left[\frac{1}{2} + \frac{\sqrt{15-2\sqrt{30}}}{2\sqrt{35}} \right], & w_3 &= \frac{49h}{12(18-\sqrt{30})} \\
 x_4 &= x_{j-1} + h \left[\frac{1}{2} + \frac{\sqrt{15+2\sqrt{30}}}{2\sqrt{35}} \right], & w_4 &= \frac{49h}{12(18+\sqrt{30})}.
 \end{aligned}
 \tag{8.12}$$

We note that this will integrate exactly piecewise polynomials of order up to 7.

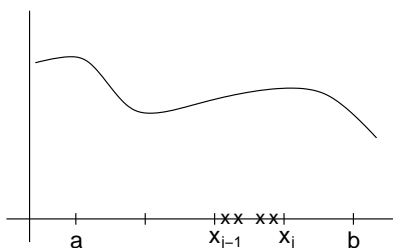


Figure 8.3. Partition of $[a, b]$ into n subintervals and position of quadrature points for the 4-point Gauss–Legendre rule on $[x_{j-1}, x_j]$.

8.1.3 2-D Quadrature Formulae

Approximation of weak formulations for plate and shell models requires the numerical evaluation of double integrals using quadrature rules of the form

$$\int_a^b \int_c^d f(x, y) dy dx \approx \sum_{i=1}^{n_x} \sum_{j=1}^{n_y} f(x_i, y_j) w_i w_j.$$

Through the change of variables

$$\begin{aligned}
 &\int_a^b \int_c^d f(x, y) dy dx \\
 &= \left(\frac{b-a}{2} \right) \left(\frac{d-c}{2} \right) \int_{-1}^1 \int_{-1}^1 f \left(\frac{a+b+\xi(b-a)}{2}, \frac{c+d+v(d-c)}{2} \right) dv d\xi,
 \end{aligned}$$

these integrals can be mapped to the rectangular domain $[-1, 1] \times [-1, 1]$ so we consider first this case. This also provides the framework necessary for numerical integration using rectangular elements. Finally, we summarize formulae for triangular elements as required for general finite element analysis.

Rectangular Domains

The formulae for rectangular domains are obtained by tensoring 1-D relations. For Gaussian formulae, this yields the nodal placement depicted in Figure 8.4.

4-Point Gauss–Legendre Quadrature

The tensor product of the 1-D formula (8.9) yields the 4-point quadrature relation

$$\int_{-1}^1 \int_{-1}^1 f(\xi, v) dv d\xi \approx f(a, a) + f(a, b) + f(b, a) + f(b, b)$$

where $a = b = \frac{1}{\sqrt{3}}$. This relation is exact for polynomials of degree 2. Hence this algorithm would be employed when integrating linear quadrilateral elements.

9-Point Gauss–Legendre Quadrature

The tensor product of the 3-point formula from Table 8.1 yields

$$\begin{aligned} \int_{-1}^1 \int_{-1}^1 f(\xi, v) dv d\xi \approx & \frac{25}{81} [f(a, a), f(a, c) + f(c, a) + f(c, c)] \\ & + \frac{40}{81} [f(a, b) + f(c, b) + f(b, a) + f(b, c)] + \frac{64}{81} f(b, b) \end{aligned}$$

where $a = -\sqrt{\frac{3}{5}}$, $b = 0$ and $c = \sqrt{\frac{3}{5}}$. This relation is exact for degree 4 polynomials so it would be used to integrate quadratic elements [390].

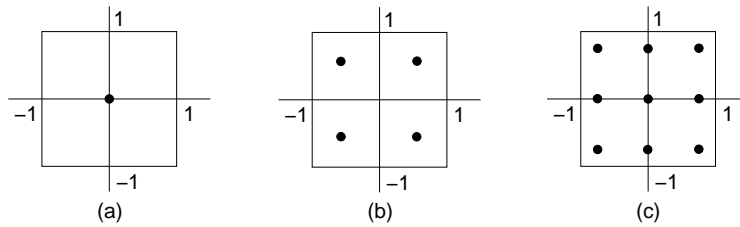


Figure 8.4. *Quadrature points in a 2-D rectangular domain: (a) 1-point rule, (b) 4-point rule, and (c) 9-point rule.*

Triangular Domains

For general finite element analysis, it is also necessary to consider quadrature formulae for triangular domains. This is often accomplished by considering transformations between physical space (x, y -coordinates) and computational space

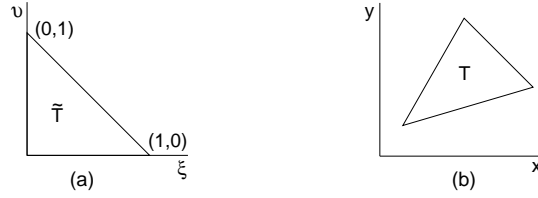


Figure 8.5. (a) Master triangular element and (b) global element in physical space.

(ξ, v -coordinates), as shown in Figure 8.5, so we summarize first the construction of local coordinates that are independent of orientation.

The local coordinates L_1, L_2 and L_3 are defined as the ratio between the perpendicular distance s to a side and the altitude h of the side as depicted in Figure 8.6(a). This implies that $0 \leq L_i \leq 1$. To elucidate a second property of the elements, consider the triangle T_1 , delineated by L_1 as shown in Figure 8.6(b), and the complete triangle T . From the area relations

$$A_{T_1} = \frac{sb}{2}, \quad A_T = \frac{hb}{2},$$

it follows that $L_1 = \frac{A_{T_1}}{A_T}$. This motivates the designation of L_1, L_2, L_3 as *area coordinates* and establishes the relation

$$L_1 + L_2 + L_3 = 1.$$

From the definition of the local coordinate L_1 , it follows that it satisfies the property

$$L_1 = \begin{cases} 1 & \text{at node } i \\ 0 & \text{at nodes } j \text{ and } k \end{cases}$$

with similar properties for L_2 and L_3 . When combined with the linearity of the definition, this implies that local coordinates also provide the simplex linear elements N_i, N_j, N_k depicted in Figure 8.7; that is,

$$N_i = L_1, \quad N_j = L_2, \quad N_k = L_3.$$

This proves crucial when defining quadrature properties for the finite element method.

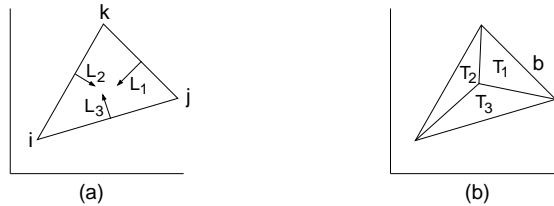


Figure 8.6. (a) Local coordinates L_1, L_2, L_3 and (b) triangles T_1, T_2, T_3 having the areas $A_{T_1}, A_{T_2}, A_{T_3}$.

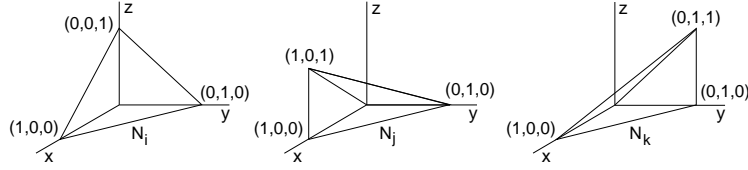


Figure 8.7. Linear elements N_i, N_j and N_k .

Letting J denote the Jacobian for the transformation between physical and master triangular elements, it follows that

$$\begin{aligned} \int_T f(x, y) dx dy &= \int_{\bar{T}} f(L_1, L_2, L_3) |J| dL_1 dL_2 \\ &\approx \frac{1}{2} \sum_{i=1}^n w_i f(L_{1_i}, L_{2_i}, L_{3_i}) |J_i|. \end{aligned}$$

The quadrature points, weights, and degrees of precision for $n = 1, 2, 3$ are summarized in Table 8.2 and higher-order formulae can be found in [205, 462].

To illustrate, the 1-point quadrature relation

$$\int_{\bar{T}} f(\xi, v) d\xi dv \approx \frac{1}{2} f(1/3, 1/3)$$

integrates linear functions exactly whereas quadratic polynomials are integrated exactly by the formula

$$\int_{\bar{T}} f(\xi, v) d\xi dv \approx \frac{1}{6} [f(1/2, 0) + f(0, 1/2) + f(1/2, 1/2)].$$

Note that all of the formulae yield the triangle area $A = \frac{1}{2}$ with $f(\xi, v) = 1$.

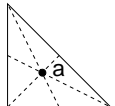
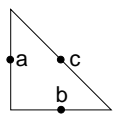
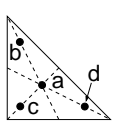
n	Degree of Precision	Local Coordinates			Weights	Geometric Location
		L_1	L_2	L_3	w	
1	1	$\frac{1}{3}$	$\frac{1}{3}$	$\frac{1}{3}$	1	a 
3	2	$\frac{1}{2}$	0	$\frac{1}{2}$	$\frac{1}{3}$	a
		$\frac{1}{2}$	$\frac{1}{2}$	0	$\frac{1}{3}$	b 
		0	$\frac{1}{2}$	$\frac{1}{2}$	$\frac{1}{3}$	c
4	3	$\frac{1}{3}$	$\frac{1}{3}$	$\frac{1}{3}$	$-\frac{27}{48}$	a
		$\frac{2}{15}$	$\frac{2}{15}$	$\frac{11}{15}$	$\frac{25}{48}$	b
		$\frac{11}{15}$	$\frac{2}{15}$	$\frac{2}{15}$	$\frac{25}{48}$	c
		$\frac{2}{15}$	$\frac{11}{15}$	$\frac{2}{15}$	$\frac{25}{48}$	d 

Table 8.2. Quadrature points and weights for triangular elements.

8.2 Numerical Approximation of the Rod Model

In this section, we illustrate approximation techniques for the distributed rod models developed in Section 7.3. For the general model (7.18), we first consider a direct Galerkin discretization in space followed by a finite difference discretization in time. This yields *global* mass, stiffness and damping matrices, a semi-discrete system appropriate for control design, and a fully discrete system feasible for simulations. Secondly, we consider an *elemental* analysis to demonstrate aspects of finite element assembly often employed for 2-D and 3-D characterization.

8.2.1 Global Discretization in Space

Consider the weak model formulation (7.18),

$$\int_0^\ell \rho A \frac{\partial^2 u}{\partial t^2} \phi dx + \int_0^\ell \left[Y A \frac{\partial u}{\partial x} + c A \frac{\partial^2 u}{\partial x \partial t} \right] \frac{d\phi}{dx} dx = \int_0^\ell f \phi dx$$

$$+ A \left[a_1 \tilde{P} + a_2 \tilde{P}^2 \right] \int_0^\ell \frac{d\phi}{dx} dx - \left[k_\ell u(t, \ell) + c_\ell \frac{\partial u}{\partial t}(t, \ell) + m_\ell \frac{\partial^2 u}{\partial t^2}(t, \ell) \right] \phi(\ell),$$
(8.13)

where $\tilde{P} = P - P_R$, which must hold for ϕ in the space of test functions

$$V = \{ \Phi = (\phi, \varphi) \in L^2(0, \ell) \times \mathbb{R} \mid \phi \in H^1(0, \ell), \phi(0) = 0, \phi(\ell) = \varphi \}.$$

The goal when constructing Galerkin solutions to (8.13) is to determine approximate solutions in finite dimensional subspaces V^N of V .

To construct V^N , we consider a uniform partition of the interval $[0, \ell]$ with points $x_j = jh, j = 0, \dots, N$ and a uniform stepsize $h = \frac{\ell}{N}$ where N denotes the number of subintervals. The spatial basis $\{\phi_j\}_{j=1}^N$ used to construct V^N is comprised of linear splines

$$\phi_j(x) = \frac{1}{h} \begin{cases} x - x_{j-1}, & x_{j-1} \leq x < x_j \\ x_{j+1} - x, & x_j \leq x \leq x_{j+1} \\ 0, & \text{otherwise} \end{cases}, \quad j = 1, \dots, N-1$$

$$\phi_N(x) = \frac{1}{h} \begin{cases} x - x_{N-1}, & x_{N-1} \leq x \leq x_N \\ 0, & \text{otherwise} \end{cases}$$
(8.14)

as depicted in Figure 8.8. It is observed that the basis functions satisfy the essential boundary condition $\phi_j(0) = 0$ for $j = 1, \dots, N$. Furthermore, $\{\phi_j\}_{j=1}^N$ are differentiable throughout $(0, \ell)$, except at the countable set of gridpoints, and hence they

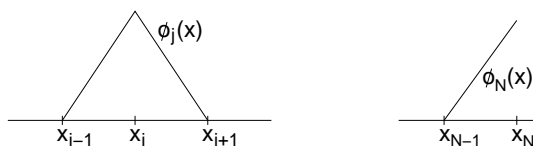


Figure 8.8. Piecewise linear basis functions (a) $\phi_j(x)$ and (b) $\phi_N(x)$.

are elements in $H^1(0, \ell)$. Letting $\varphi_j = \phi_j(\ell)$ and $\Phi_j = (\phi_j, \varphi_j)$, the approximating subspace is defined to be

$$V^N = \text{span} \{ \Phi_j \}.$$

The solution to (8.13) is approximated by the expansion

$$u^N(t, x) = \sum_{j=1}^N u_j(t) \phi_j(x) \tag{8.15}$$

which satisfies $u^N(t, 0) = 0$ and can achieve arbitrary displacements at $x = \ell$.

A semi-discrete second-order matrix system is obtained by considering the approximate solution $u^N(t, x)$ in (8.13) with the basis functions $\{ \phi_i \}_{i=1}^N$ employed as test functions — this is equivalent to projecting the system (8.13) onto the finite-dimensional subspace V^N . The interchange of integration and summation yields the system

$$\begin{aligned} & \sum_{j=1}^N \ddot{u}_j(t) \int_0^\ell \rho A \phi_i \phi_j dx + \sum_{j=1}^N \dot{u}_j(t) \int_0^\ell c A \phi_i' \phi_j' dx + \sum_{j=1}^N u_j(t) \int_0^\ell Y A \phi_i' \phi_j' dx \\ &= \int_0^\ell f \phi_i dx + A [a_1(P - P_R) + a_2(P - P_R)^2] \int_0^\ell \phi_i' dx \\ & - \left(k_\ell u_N(t) \phi_N(\ell) + c_\ell \dot{u}_N(t) \phi_N(\ell) + m_\ell \ddot{u}_N(t) \phi_N(\ell) \right) \phi_N(\ell) \end{aligned}$$

which holds for $i = 1, \dots, N$. This can be written as the second-order vector-valued system

$$\mathbb{M} \ddot{\mathbf{u}}(t) + \mathbb{Q} \dot{\mathbf{u}} + \mathbb{K} \mathbf{u}(t) = \mathbf{f}(t) + A [a_1(P(E(t)) - P_R) + a_2(P(E(t)) - P_R)^2] \mathbf{b} \tag{8.16}$$

where

$$\mathbf{u}(t) = [u_1(t), \dots, u_N(t)]^T.$$

The *global* mass, stiffness and damping matrices have the components

$$\begin{aligned} [\mathbb{M}]_{ij} &= \begin{cases} \int_0^\ell \rho A \phi_i \phi_j dx & , \quad i \neq N \text{ or } j \neq N \\ \int_0^\ell \rho A \phi_i \phi_j dx + m_\ell & , \quad i = N \text{ and } j = N \end{cases} \\ [\mathbb{K}]_{ij} &= \begin{cases} \int_0^\ell Y A \phi_i' \phi_j' dx & , \quad i \neq N \text{ or } j \neq N \\ \int_0^\ell Y A \phi_i' \phi_j' dx + k_\ell & , \quad i = N \text{ and } j = N \end{cases} \\ [\mathbb{Q}]_{ij} &= \begin{cases} \int_0^\ell c A \phi_i' \phi_j' dx & , \quad i \neq N \text{ or } j \neq N \\ \int_0^\ell c A \phi_i' \phi_j' dx + c_\ell & , \quad i = N \text{ and } j = N \end{cases} \end{aligned} \tag{8.17}$$

whereas the force vectors are defined by

$$[\mathbf{f}]_i = \int_0^\ell f \phi_i dx \quad , \quad [\mathbf{b}]_i = \int_0^\ell \phi_i' dx. \quad (8.18)$$

To evaluate the integrals, it is observed that when ρ and Y are constant, the maximal degree occurs in the mass matrix which is comprised of quadratic polynomials on each subinterval $[x_{j-1}, x_j]$. In this case, 2-point composite Gaussian quadrature with nodes and weights

$$\begin{aligned} x_1 &= x_{j-1} + \frac{h}{2} \left(1 - 1/\sqrt{3}\right) \quad , \quad w_1 = \frac{h}{2} \\ x_2 &= x_{j-1} + \frac{h}{2} \left(1 + 1/\sqrt{3}\right) \quad , \quad w_2 = \frac{h}{2} \end{aligned}$$

will provide *exact* integration on $[x_{j-1}, x_j]$ which yields the tridiagonal matrices

$$\mathbb{M} = \rho Ah \begin{bmatrix} \frac{2}{3} & \frac{1}{6} & 0 & \cdots & 0 \\ \frac{1}{6} & \frac{2}{3} & \frac{1}{6} & & \\ & \ddots & \ddots & \ddots & \\ & & \frac{1}{6} & \frac{2}{3} & \frac{1}{6} \\ 0 & \cdots & 0 & \frac{1}{6} & \frac{1}{3} + \frac{m_\ell}{h} \end{bmatrix} \quad , \quad \mathbb{K} = \frac{YA}{h} \begin{bmatrix} 2 & -1 & 0 & \cdots & 0 \\ -1 & 2 & -1 & & \\ & \ddots & \ddots & \ddots & \\ & & -1 & 2 & -1 \\ 0 & \cdots & 0 & -1 & 1 + hk_\ell \end{bmatrix} \quad (8.19)$$

and vector

$$\mathbf{b} = [0, \dots, 1]^T.$$

The damping matrix has the representation $\mathbb{Q} = \frac{c}{Y} \mathbb{K}$ when c is constant.

To formulate a first-order semi-discrete system appropriate for finite-dimensional control design, we let $\mathbf{z} = [\mathbf{u}, \dot{\mathbf{u}}]^T$ and define the system matrix \mathbb{A} and vectors $\mathbf{F}(t)$ and \mathbf{B} by

$$\begin{aligned} \mathbb{A} &= \begin{bmatrix} 0 & \mathbb{I} \\ -\mathbb{M}^{-1}\mathbb{K} & -\mathbb{M}^{-1}\mathbb{Q} \end{bmatrix}, \\ \mathbf{F}(t) &= \begin{bmatrix} 0 \\ \mathbb{M}^{-1}\mathbf{f}(t) \end{bmatrix} \quad , \quad \mathbf{B} = \begin{bmatrix} 0 \\ \mathbb{M}^{-1}\mathbf{b} \end{bmatrix}. \end{aligned} \quad (8.20)$$

The second-order system (8.16) can subsequently be reformulated as

$$\begin{aligned} \dot{\mathbf{z}}(t) &= \mathbb{A} \mathbf{z}(t) + \mathbf{F}(t) + A [a_1(P(E(t)) - P_R) + a_2(P(E(t)) - P_R)^2] \mathbf{B} \\ \mathbf{z}(0) &= \mathbf{z}_0 \end{aligned} \quad (8.21)$$

where the $2N \times 1$ vector \mathbf{z}_0 denotes the projection of the initial conditions into the approximating subspace.

Temporal Discretization

The system (8.21) must be discretized in time to permit numerical or experimental implementation. The choice of approximation method is dictated by

accuracy and stability requirements, storage capabilities, and sample rates. This can be accomplished using MATLAB routines such as `ode15s.m` which accommodate the moderate stiffness inherent to Galerkin approximation in space. Alternatively, a trapezoidal method can be advantageous for experimental implementation since it is moderately accurate, is A-stable, and requires minimal storage when implemented as a single step method. For temporal stepsizes Δt , a standard trapezoidal discretization yields the iteration

$$\begin{aligned} \mathbf{z}_{k+1} &= \mathbb{W}\mathbf{z}_k + \frac{1}{2}\mathbb{V}[\mathbf{F}(t_k) + \mathbf{F}(t_{k+1})] \\ &\quad + \frac{1}{2} \left[a_1 \tilde{P}(E(t_k)) + a_1 \tilde{P}(E(t_{k+1})) + a_2 \tilde{P}^2(E(t_k)) + a_2 \tilde{P}^2(E(t_{k+1})) \right] \mathbb{V}\mathbf{B} \\ \mathbf{z}_0 &= \mathbf{z}(0) \end{aligned}$$

where $\tilde{P}(E) = P(E) - P_R$, $t_k = k\Delta t$, and \mathbf{z}_k approximates $\mathbf{z}(t_k)$. The matrices

$$\mathbb{W} = \left(\mathbb{I} - \frac{\Delta t}{2}\mathbb{A} \right)^{-1} \left(\mathbb{I} + \frac{\Delta t}{2}\mathbb{A} \right), \quad \mathbb{V} = \Delta t \left(\mathbb{I} - \frac{\Delta t}{2}\mathbb{A} \right)^{-1}$$

need only be created once when numerically or experimentally implementing the method. This yields approximate solutions having $\mathcal{O}(h^2, (\Delta t)^2)$ accuracy. For applications in which data at future times t_{k+1} is unavailable, the modified trapezoidal algorithm

$$\begin{aligned} \mathbf{z}_{k+1} &= \mathbb{W}\mathbf{z}_k + \mathbb{V}\mathbf{F}(t_k) + [a_1(P(E(t_k)) - P_R) + a_2(P(E(t_k)) - P_R)^2] \mathbb{V}\mathbf{B} \\ \mathbf{z}_0 &= \mathbf{z}(0) \end{aligned}$$

can be employed. Whereas this decreases slightly the temporal accuracy, for large sample rates with correspondingly small stepsizes Δt , the accuracy is still commensurate with that of the data.

Remark 8.2.1. *The approximation of the eigenvalue problem associated with the undamped rod model yields the generalized eigenvalue problem*

$$\mathbb{K}\boldsymbol{\zeta} = \omega^2\mathbb{M}\boldsymbol{\zeta} \tag{8.22}$$

where the stiffness matrix \mathbb{K} and mass matrix \mathbb{M} are defined in (8.19). Hence (8.22) can be used to approximate the natural frequencies and modes for the undamped rod.

Remark 8.2.2. *Due to the presence of both internal damping and damping in the boundary condition at $x = \ell$, the eigenvalues of the system matrix \mathbb{A} defined in (8.20) will all have negative real part. This property can be used to check the validity of the signs in the boundary condition (7.13) and weak formulation (8.13). For example, an incorrect formulation which added rather than subtracted the final boundary contribution will produce eigenvalues of \mathbb{A} having positive real part which is inconsistent with the damping in the model.*

8.2.2 Elemental Analysis

The spatial discretization technique detailed in Section 8.2.1 illustrates the general philosophy of Galerkin approximation including the definition of global basis functions and their use for defining an approximating subspace $V^N \subset V$. In this section, we summarize a local, elemental approach to the problem. Whereas the two techniques yield equivalent mass, stiffness and damping matrices, the latter is significantly more efficient for general 2-D and 3-D geometries and hence is employed for general finite element analysis of complex structures.

To simplify the discussion and facilitate energy analysis, we consider the regime employed in Section 7.3.2 and take $c = f = P = m_\ell = c_\ell = k_\ell = 0$ in the weak formulation (8.13). Additionally, we assume that ρ and Y are constant. This model quantifies the dynamics of an undamped and unforced rod that is fixed at $x = 0$ and free at $x = \ell$. The space of test functions in this case is

$$V = H_0^1(0, \ell) = \{ \phi \in H^1(0, \ell) \mid \phi(0) = 0 \}.$$

Local Basis Elements

To illustrate the construction of local mass and stiffness matrices, we initially consider the approximation of rod dynamics on a local interval $[0, h]$ as depicted in Figure 8.9(a). In accordance with the assumption that u is differentiable in x at all but a countable number of points, we express displacements as

$$\begin{aligned} u(t, x) &= a_0(t) + a_1(t)x \\ &= \boldsymbol{\varphi}^T(x)\mathbf{a}(t) \end{aligned}$$

where $\mathbf{a}(t) = [a_0(t), a_1(t)]^T$ and $\boldsymbol{\varphi}(x) = [1, x]^T$. To formulate u in terms of the nodal values $u_\ell(t)$ and $u_r(t)$ at $x = 0$ and $x = h$, we note that

$$\begin{bmatrix} u_\ell(t) \\ u_r(t) \end{bmatrix} = \begin{bmatrix} 1 & 0 \\ 1 & h \end{bmatrix} \begin{bmatrix} a_0(t) \\ a_1(t) \end{bmatrix}$$

or

$$\mathbf{u}(t) = \mathbb{T}\mathbf{a}(t)$$

where

$$\mathbb{T} = \begin{bmatrix} 1 & 0 \\ 1 & h \end{bmatrix}, \quad \mathbf{u}(t) = \begin{bmatrix} u_\ell(t) \\ u_r(t) \end{bmatrix}.$$



Figure 8.9. (a) Rod displacements $u_\ell(t)$ and $u_r(t)$ at the left and right endpoints of the local interval $[0, h]$. (b) Local linear basis functions $\tilde{\phi}_1(x)$ and $\tilde{\phi}_2(x)$.

By observing that $\mathbf{a}(t) = \mathbb{S}\mathbf{u}(t)$, where

$$\mathbb{S} = \mathbb{T}^{-1} = \begin{bmatrix} 1 & 0 \\ -\frac{1}{h} & \frac{1}{h} \end{bmatrix},$$

it follows that displacements can be represented as

$$u(t, x) = \boldsymbol{\phi}^T(x)\mathbf{u}(t). \tag{8.23}$$

Here $\boldsymbol{\phi}(x) = [\tilde{\phi}_1(x), \tilde{\phi}_2(x)]^T$ contains the *local basis elements*

$$\tilde{\phi}_1(x) = 1 - \frac{x}{h}, \quad \tilde{\phi}_2(x) = \frac{x}{h}$$

depicted in Figure 8.9(b).

Note that (8.23) is a local version of the expansion (8.15) employed when constructing approximate solutions using the global basis functions $\{\phi_j\}_{j=1}^N$ defined in (8.14). The local region $[0, h]$ and global interval $[x_{j-1}, x_j]$ are analogous to the master and physical triangles depicted in Figure 8.5 whereas the local basis set $\{\tilde{\phi}_1, \tilde{\phi}_2\}$ is the 1-D analogue of the 2-D elements $\{N_i, N_j, N_k\}$ shown in Figure 8.7.

Hamiltonian Formulation

To specify a dynamic model quantifying the displacements u , we employ the Hamiltonian framework detailed in Section 7.3.2 for the infinite dimensional problem. Here we consider displacements $u \in V^N = \text{span}\{\tilde{\phi}_1, \tilde{\phi}_2\}$ as dictated by our approximation framework.

We first note that for this class of displacements, the squared strains and velocities can be expressed as

$$\begin{aligned} u_x^2(t, x) &= \mathbf{u}^T(t)\mathbb{S}^T\mathbb{D}(x)\mathbb{S}\mathbf{u}(t) \\ u_t^2(t, x) &= \dot{\mathbf{u}}^T(t)\mathbb{S}^T\mathbb{F}(x)\mathbb{S}\dot{\mathbf{u}}(t) \end{aligned}$$

where

$$\mathbb{D}(x) = \boldsymbol{\varphi}_x(x)\boldsymbol{\varphi}_x^T(x)^T = \begin{bmatrix} 0 & 0 \\ 0 & 1 \end{bmatrix}, \quad \mathbb{F}(x) = \boldsymbol{\varphi}(x)\boldsymbol{\varphi}^T(x) = \begin{bmatrix} 1 & x \\ x & x^2 \end{bmatrix}.$$

The potential and kinetic energies (7.20) can thus be expressed as

$$\begin{aligned} U &= \frac{YA}{2}\mathbf{u}^T(t)\mathbb{S}^T \cdot \int_0^h \mathbb{D}(x)dx \cdot \mathbb{S}\mathbf{u}(t) \\ K &= \frac{\rho A}{2}\dot{\mathbf{u}}^T(t)\mathbb{S}^T \cdot \int_0^h \mathbb{F}(x)dx \cdot \mathbb{S}\dot{\mathbf{u}}(t). \end{aligned}$$

Application of Hamilton's principle in the manner detailed in Section 7.3.2 yields the relation

$$\rho AS^T \cdot \int_0^h \mathbb{F}(x)dx \cdot \mathbb{S}\ddot{\mathbf{u}}(t) + YAS^T \cdot \int_0^h \mathbb{D}(x)dx \cdot \mathbb{S}\mathbf{u}(t) = 0. \tag{8.24}$$

Local Mass and Stiffness Matrices

The weak formulation (8.24) can be written as

$$\mathbb{M}_e \ddot{\mathbf{u}}(t) + \mathbb{K}_e \mathbf{u} = 0$$

where

$$\mathbb{M}_e = \rho A \mathbb{S}^T \cdot \int_0^h \mathbb{F}(x) dx \cdot \mathbb{S} \quad , \quad \mathbb{K}_e = Y A \mathbb{S}^T \cdot \int_0^h \mathbb{D}(x) dx \cdot \mathbb{S}$$

are the *local* mass and stiffness matrices. Evaluation of the integrals yields the analytic formulations

$$\mathbb{M}_e = \rho A h \begin{bmatrix} \frac{1}{3} & \frac{1}{6} \\ \frac{1}{6} & \frac{1}{3} \end{bmatrix} \quad , \quad \mathbb{K}_e = \frac{Y A}{h} \begin{bmatrix} 1 & -1 \\ -1 & 1 \end{bmatrix} .$$

Global Mass and Stiffness Matrices

To motivate the techniques used to construct global mass and stiffness matrices, we first partition the rod interval $[0, \ell]$ into two subregions as shown in Figure 8.10(a) — hence $h = \frac{\ell}{2}$. With the requirement that $u_{1r}(t) = u_{2\ell}(t)$, the nodal unknowns in this case are $\mathbf{u}(t) = [u_{1\ell}(t), u_{2\ell}(t), u_{2r}(t)]^T$. Combination of the local relations subsequently yields the global system

$$\mathbb{M} \ddot{\mathbf{u}} + \mathbb{K} \mathbf{u} = 0$$

where the *global* mass and stiffness matrices are given by

$$\mathbb{M} = \rho A h \begin{bmatrix} \frac{1}{3} & \frac{1}{6} & 0 \\ \frac{1}{6} & \frac{2}{3} & \frac{1}{6} \\ 0 & \frac{1}{6} & \frac{1}{3} \end{bmatrix} \quad , \quad \mathbb{K} = \frac{Y A}{h} \begin{bmatrix} 1 & -1 & 0 \\ -1 & 2 & -1 \\ 0 & -1 & 1 \end{bmatrix} .$$

We note that the second row in the mass matrix is obtained by summing the element relations

$$\begin{aligned} \frac{\rho A \ell}{2} \left(\frac{1}{6} \ddot{u}_{1\ell} + \frac{1}{3} \ddot{u}_{2\ell} \right) &= 0 \\ \frac{\rho A \ell}{2} \left(\frac{1}{3} \ddot{u}_{2\ell} + \frac{1}{6} \ddot{u}_{2r} \right) &= 0 \end{aligned}$$

after enforcing $\ddot{u}_{1r} = \ddot{u}_{2\ell}$. A similar strategy is employed when constructing the stiffness matrix and the general procedure is illustrated in Figure 8.11(a).



Figure 8.10. Partition of the rod domain $[0, \ell]$ into (a) 2 subregions and (b) n subregions.

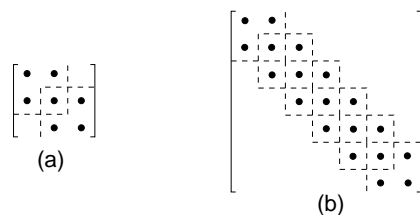


Figure 8.11. Combination of elemental mass and stiffness matrices \mathbb{M}_e and \mathbb{K}_e to construct global matrices \mathbb{M} and \mathbb{K} : (a) 2 subregions, and (b) n subregions.

The process for general partitions $x_j = jh, j = 0, 1, \dots, N$ with $h = \frac{\ell}{N}$ is identical and leads to a similar summation process as shown in Figure 8.11(b). Enforcing the boundary condition $u_{1\ell} = 0$ subsequently yields the global mass and stiffness matrices

$$\mathbb{M} = \rho Ah \begin{bmatrix} \frac{2}{3} & \frac{1}{6} & 0 & \cdots & 0 \\ \frac{1}{6} & \frac{2}{3} & \frac{1}{6} & & \\ & \ddots & \ddots & \ddots & \\ & & \frac{1}{6} & \frac{2}{3} & \frac{1}{6} \\ 0 & \cdots & 0 & \frac{1}{6} & \frac{1}{3} \end{bmatrix}, \quad \mathbb{K} = \frac{YA}{h} \begin{bmatrix} 2 & -1 & 0 & \cdots & 0 \\ -1 & 2 & -1 & & \\ & \ddots & \ddots & \ddots & \\ & & -1 & 2 & -1 \\ 0 & \cdots & 0 & -1 & 1 \end{bmatrix}. \quad (8.25)$$

A comparison between (8.25) and (8.19) obtained through global analysis illustrates that the matrices are identical when one takes $m_\ell = k_\ell = 0$ in the latter set.

The technique can be extended to incorporate linear and nonlinear inputs by employing the augmented action integral (7.25) and an extended Hamilton's principle. Internal and boundary damping is incorporated by employing extended constitutive relations as detailed in the previous section.

Whereas the global discretization techniques and elemental analysis provide the same semi-discrete systems, the latter technique facilitates implementation for general 2-D and 3-D geometries discretized using triangular meshes. Additional details regarding finite element techniques for rod models can be found in [36, 276].

8.2.3 Examples and Software

The performance of the discretized rod model is illustrated in Section 7.3.3 in the context of characterizing displacements generated by a stacked PZT actuator from an AFM stage. This example illustrates the effects of variable drive levels and the incorporation of frequency-dependent hysteresis mechanisms via the nonlinear constitutive relations developed in Chapter 2.

The performance of the approximation techniques when used to characterize the hysteretic dynamics of a Terfenol-D transducer is reported in [119, 120]. In this case, the domain wall model was used to provide the constitutive relations which provide the basis for constructing the distributed rod model. In both cases, the mass, stiffness and damping matrices have the general representations (8.17) —

\mathbb{M} and \mathbb{K} have the specific representations (8.19) when ρ and Y are constant — and the input vectors are given by (8.18). The only differences in the models occur in the scalar-valued input relations used to characterize the nonlinear hysteresis.

MATLAB m-files for implementing both the rod model and the model for the stacked PZT actuator employed in the AFM stage can be found at the website <http://www.siam.org/books/fr32>.

8.3 Numerical Approximation of the Beam Model

The strategy for approximating the beam models developed in Section 7.4 is analogous to that employed for the rod models — spline or finite element discretizations in space are used to construct semi-discrete systems appropriate for control design or subsequent temporal discretization for simulations. Unlike rod models, quantification of the bending moments or strain energy associated with bending yields second derivatives in weak beam formulations which must be accommodated by basis functions. In Section 8.3.1 we summarize the use of cubic B-splines to construct approximating subspaces whereas a cubic Hermite basis is constructed in Section 8.3.2 through techniques analogous to those of Section 8.2.2.

8.3.1 Cubic Spline Basis

We illustrate beam approximation in the context of a cantilever beam, having a fixed-end at $x = 0$ and free-end at $x = \ell$, with surface-mounted patches. For test functions ϕ in the space

$$V = H_0^2(0, \ell) = \{ \phi \in H^2(0, \ell) \mid \phi(0) = \phi'(0) = 0 \},$$

the weak formulation of the model for linear inputs is

$$\begin{aligned} \int_0^\ell \rho \frac{\partial^2 w}{\partial t^2} \phi dx + \gamma \int_0^\ell \frac{\partial w}{\partial t} \phi dx + \int_0^\ell YI \frac{\partial^2 w}{\partial x^2} \frac{d^2 \phi}{dx^2} dx \\ + \int_0^\ell cI \frac{\partial^3 w}{\partial x^2 \partial t} \frac{d^2 \phi}{dx^2} dx = \int_0^\ell f \phi dx + V(t) \int_0^\ell k_p \frac{d^2 \phi}{dx^2} dx \end{aligned} \tag{8.26}$$

where the piecewise constants ρ, YI, cI and k_p are defined in (7.42) and (7.44).

To formulate approximate solutions based on cubic B-Splines, consider the partition $x_j = jh$, where $h = \frac{\ell}{N}$ and $j = 0, \dots, N$. For $j = -1, 0, 1, \dots, N + 1$, it is shown in [383] that standard cubic B-splines are defined by

$$\widehat{\phi}_j(x) = \frac{1}{h^3} \begin{cases} (x - x_{j-2})^3, & x \in [x_{j-2}, x_{j-1}) \\ h^3 + 3h^2(x - x_{j-1}) + 3h(x - x_{j-1})^2 - 3(x - x_{j-1})^3, & x \in [x_{j-1}, x_j) \\ h^3 + 3h^2(x_{j+1} - x) + 3h(x_{j+1} - x)^2 - 3(x_{j+1} - x)^3, & x \in [x_j, x_{j+1}) \\ (x_{j+2} - x)^3, & x \in [x_{j+1}, x_{j+2}) \\ 0, & \text{otherwise} \end{cases} \tag{8.27}$$

as illustrated in Figure 8.12. To accommodate the essential boundary conditions $w(t, 0) = \frac{\partial w}{\partial x}(t, 0) = 0$ and corresponding restrictions $\phi(0) = \phi'(0) = 0$ required of functions in V , we employ the basis functions

$$\phi_j(x) = \begin{cases} \widehat{\phi}_0(x) - 2\widehat{\phi}_{-1}(x) - 2\widehat{\phi}_1(x) & , \quad j = 1 \\ \widehat{\phi}_j(x) & , \quad j = 2, \dots, N + 1 \end{cases} \quad (8.28)$$

which are modified to ensure that $\phi_j \in V$ for $j = 1, \dots, N + 1$. Finally, we consider approximate solutions

$$w^N(t, x) = \sum_{j=1}^{N+1} w_j(t) \phi_j(x)$$

in the space $V^N = \text{span}\{\phi_j\} \subset V$.

In a manner similar to that detailed in Section 8.2.1, consideration of w^N in (8.26) with basis functions employed as test functions yields the semi-discrete system

$$\mathbb{M} \ddot{\mathbf{w}} + \mathbb{Q} \dot{\mathbf{w}} + \mathbb{K} \mathbf{w} = \mathbf{f} + V(t)\mathbf{b} \quad (8.29)$$

where

$$\mathbf{w}(t) = [w_1(t), \dots, w_{N+1}(t)]^T. \quad (8.30)$$

The *global* mass, damping and stiffness matrices are defined by

$$\begin{aligned} [\mathbb{M}]_{ij} &= \int_0^\ell \rho \phi_i \phi_j dx \\ [\mathbb{Q}]_{ij} &= \int_0^\ell [\gamma \phi_i \phi_j + cI \phi_i'' \phi_j''] dx \\ [\mathbb{K}]_{ij} &= \int_0^\ell YI \phi_i'' \phi_j'' dx \end{aligned} \quad (8.31)$$

whereas the force vectors have the components

$$[\mathbf{f}]_i = \int_0^\ell f \phi_i dx \quad , \quad [\mathbf{b}]_i = \int_0^\ell \phi_i'' dx. \quad (8.32)$$

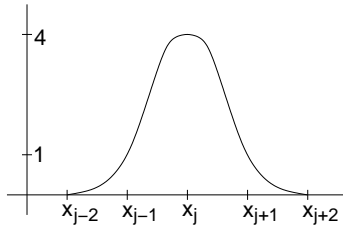


Figure 8.12. Cubic B-spline $\phi_j(x)$.

A more pertinent issue arises when addressing the problem of *optimal patch location* for which x_1 and x_2 are parameters determined through an optimization routine [132, 155, 202]. This necessitates consideration of variable or adaptive meshes and constitutes an active research area.

Projection Method

It is important to note that approximation using the modified B-spline basis (8.28) constitutes a projection rather than interpolation method as is the case for the cubic Hermite methods summarized in Section 8.3.2. Hence the coefficients (8.30) do not approximate nodal values of the true solution and modified basis functions are required to accommodate essential boundary conditions. In this sense, B-spline approximation shares a projective kinship with globally defined spectral methods — e.g., Legendre or Fourier — while retaining the sparsity associated with locally defined polynomial elements. As will be detailed in Section 8.3.3, the advantage of cubic B-splines over cubic Hermite elements lies in the fact that half as many coefficients are required in the former case. The non-interpolatory nature of B-splines constitutes the primary disadvantage which is especially pertinent when accommodating boundary or interface conditions between components of the structure — e.g., curved and flat portions of THUNDER transducers.

8.3.2 Cubic Hermite Basis

To illustrate the construction of a finite element basis which interpolates displacements and slopes at the partition points, we initially consider the model (8.26) in the absence of internal or air damping and external forces — hence $c = \gamma = f = V = 0$. Additionally, we take ρ and Y to be constant to highlight the structure of constituent matrices.

Local Mass and Stiffness Matrices

It was detailed in Section 7.4 that thin beam models quantify both the transverse displacement and rotation of the neutral line so we begin the elemental analysis by quantifying the displacements w_ℓ, w_r and slopes θ_ℓ, θ_r on an arbitrary interval $[0, h]$ as depicted in Figure 8.13. Once we have constructed local mass and stiffness matrices, we will extend the analysis to partitions of the full beam interval $[0, \ell]$ to construct global system matrices.

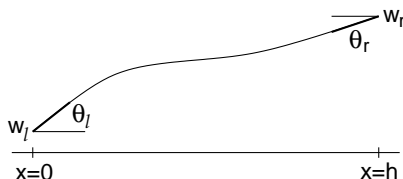


Figure 8.13. Displacements w_ℓ, w_r and slopes θ_ℓ, θ_r at the ends of a cubic element on the interval $[0, h]$.

Because the characterization of $\mathbf{w}(t) = [w_\ell(t), \theta_\ell(t), w_r(t), \theta_r(t)]^T$ involves 4 degrees of freedom, we consider cubic representations

$$\begin{aligned} w(t, x) &= a_0(t) + a_1(t)x + a_2(t)x^2 + a_3(t)x^3 \\ &= \boldsymbol{\varphi}^T(x)\mathbf{a}(t) \end{aligned} \tag{8.33}$$

where $\mathbf{a}(t) = [a_0(t), a_1(t), a_2(t), a_3(t)]^T$ and $\boldsymbol{\varphi}(x) = [1, x, x^2, x^3]^T$. By noting that $\theta(t, x) = \frac{\partial w}{\partial x}(t, x)$ and enforcing the interpolation conditions at $x = 0$ and h , the nodal coefficients can be represented as

$$\mathbf{w}(t) = \mathbb{T}\mathbf{a}(t)$$

where

$$\mathbb{T} = \begin{bmatrix} 1 & 0 & 0 & 0 \\ 0 & 1 & 0 & 0 \\ 1 & h & h^2 & h^3 \\ 0 & 1 & 2h & 3h^2 \end{bmatrix}.$$

Substitution of $\mathbf{a}(t) = \mathbb{T}^{-1}\mathbf{w}(t)$ into (8.33) yields the expansion

$$w(t, x) = \boldsymbol{\phi}^T(x)\mathbf{w}(t)$$

where $\boldsymbol{\phi} = [\tilde{\phi}_1, \tilde{\phi}_2, \tilde{\phi}_3, \tilde{\phi}_4]^T$ comprises the local cubic Hermite basis functions

$$\begin{aligned} \tilde{\phi}_1(x) &= \frac{1}{h^3}(h-x)^2[2x+h] & , & & \tilde{\phi}_3(x) &= \frac{1}{h^3}x^2[2(h-x)+h] \\ \tilde{\phi}_2(x) &= \frac{1}{h^2}x(x-h)^2 & , & & \tilde{\phi}_4(x) &= \frac{1}{h^2}x^2(x-h). \end{aligned} \tag{8.34}$$

As shown in Figure 8.14, the elements $\tilde{\phi}_j(x)$ have displacement or slope values of 0 or 1 at $x = 0, h$. This ensures that the coefficients $\mathbf{w}(t) = [w_\ell(t), \theta_\ell(t), w_r(t), \theta_r(t)]^T$ interpolate the beam displacements and slopes at $x = 0, h$.

From the relations

$$U = \frac{1}{2}YI \int_0^h \left(\frac{\partial^2 w}{\partial x^2}\right)^2 dx \quad , \quad K = \frac{1}{2}\rho \int_0^h \left(\frac{\partial^2 w}{\partial t^2}\right)^2 dx$$

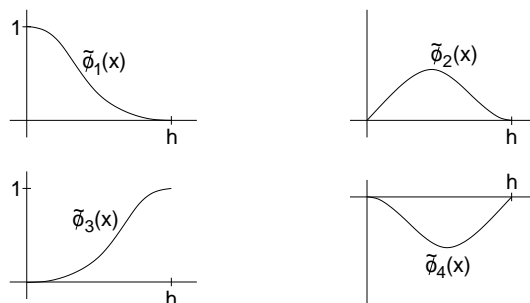


Figure 8.14. Cubic Hermite basis functions $\tilde{\phi}_1, \dots, \tilde{\phi}_4$.

for the potential energy due to bending and kinetic energy, it follows that for the class of approximate displacements (8.33),

$$U = \frac{YI}{2} \mathbf{w}^T(t) \mathbb{S}^T \cdot \int_0^h \mathbb{D}(x) dx \cdot \mathbb{S} \mathbf{w}(t)$$

$$K = \frac{\rho}{2} \dot{\mathbf{w}}^T(t) \mathbb{S}^T \cdot \int_0^h \mathbb{F}(x) dx \cdot \mathbb{S} \dot{\mathbf{w}}(t)$$

where $\mathbb{S} = \mathbb{T}^{-1}$ and

$$\mathbb{D}(x) = \varphi_{xx}(x) \varphi_{xx}^T(x) = \begin{bmatrix} 0 & 0 & 0 & 0 \\ 0 & 0 & 0 & 0 \\ 0 & 0 & 4 & 12x \\ 0 & 0 & 12x & 36x^2 \end{bmatrix}$$

$$\mathbb{F}(x) = \varphi(x) \varphi^T(x) = \begin{bmatrix} 1 & x & x^2 & x^3 \\ x & x^2 & x^3 & x^5 \\ x^2 & x^3 & x^4 & x^5 \\ x^3 & x^4 & x^5 & x^6 \end{bmatrix}.$$

Application of Hamilton's principle in the manner detailed in Section 7.3.2 yields the second-order vector system

$$\mathbb{M}_e \ddot{\mathbf{w}} + \mathbb{K}_e \mathbf{w} = 0$$

where the local mass and stiffness matrices are

$$\mathbb{M}_e = \frac{\rho h}{420} \begin{bmatrix} 156 & 22h & 54 & -13h \\ 22h & 4h^2 & 13h & -3h^2 \\ 54 & 13h & 156 & -22h \\ -13h & -3h^2 & -22h & 4h^2 \end{bmatrix}, \quad \mathbb{K}_e = \frac{YI}{h^3} \begin{bmatrix} 12 & 6h & -12 & 6h \\ 6h & 4h^2 & -6h & 2h^2 \\ -12 & -6h & 12 & -6h \\ 6h & 2h^2 & -6h & 4h^2 \end{bmatrix}.$$

Global Mass and Stiffness Matrices

Global mass and stiffness matrices are constructed by combining local relations subject to the constraint that displacements and slopes match at the interfaces. To illustrate, we first subdivide the beam support $[0, \ell]$ into two subregions as depicted in Figure 8.10(a). By enforcing the interface conditions

$$w_{1r}(t) = w_{2\ell}(t) \quad , \quad \theta_{1r}(t) = \theta_{2\ell}(t),$$

we obtain the global matrices

$$\mathbb{M} = \frac{\rho h}{420} \begin{bmatrix} 156 & 22h & 54 & -13h & 0 & 0 \\ 22h & 4h^2 & 13h & -3h^2 & 0 & 0 \\ 54 & 13h & 312 & 0 & 54 & -13h \\ -13h & -3h^2 & 0 & 8h^2 & 13h & -3h^2 \\ 0 & 0 & 54 & 13h & 156 & -22h \\ 0 & 0 & -13h & -3h^2 & -22h & 4h^2 \end{bmatrix}$$

and

$$\mathbb{K} = \frac{YI}{h^3} \begin{bmatrix} 12 & 6h & -12 & 6h & 0 & 0 \\ 6h & 4h^2 & -6h & 2h^2 & 0 & 0 \\ -12 & -6h & 24 & 0 & -12 & 6h \\ 6h & 2h^2 & 0 & 8h^2 & -6h & 2h^2 \\ 0 & 0 & -12 & -6h & 12 & -6h \\ 0 & 0 & 6h & 2h^2 & -6h & 4h^2 \end{bmatrix}$$

where $h = \frac{\ell}{2}$.

Due to the fixed-end conditions at $x = 0$, it follows that $w_{1\ell} = \theta_{1\ell} = 0$. After re-ordering the vector of nodal values as

$$\mathbf{w}(t) = [w_{1r}(t), w_{2r}(t), \theta_{1r}(t), \theta_{2r}(t)]^T,$$

the dynamics are quantified by the system

$$\mathbb{M}\ddot{\mathbf{w}} + \mathbb{K}\mathbf{w} = 0$$

where

$$\mathbb{M} = \frac{\rho h}{420} \begin{bmatrix} 312 & 54 & 0 & -13h \\ 54 & 156 & 13h & -22h \\ 0 & 13h & 8h^2 & -3h^2 \\ -13h & -22h & -3h^2 & 4h^2 \end{bmatrix}, \quad \mathbb{K} = \frac{YI}{h^3} \begin{bmatrix} 24 & -12 & 0 & 6h \\ -12 & 12 & -6h & -6h \\ 0 & -6h & 8h^2 & 2h^2 \\ 6h & -6h & 2h^2 & 4h^2 \end{bmatrix}. \quad (8.35)$$

The process for general partitions $x_j = jh$ with $h = \frac{\ell}{N}$ is analogous and leads to a similar summation process when constructing global system matrices — see Figure 8.15. As detailed in previous sections, internal damping can be incorporated by employing more general constitutive relations based on the assumption that stress is proportional to a linear combination of strain and strain rate.

Global Discretization

We illustrated in Section 8.2 that either global Galerkin techniques or local elemental analysis could be employed when implementing linear finite element methods. The same is true with cubic Hermite elements. Whereas the local elemental analysis illustrates the implementation philosophy for general 2-D and 3-D

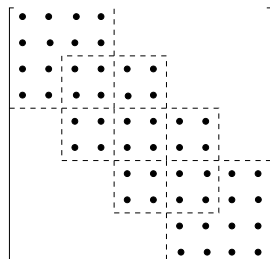


Figure 8.15. Combination of elemental mass and stiffness matrices \mathbb{M}_e and \mathbb{K}_e to construct global matrices \mathbb{M} and \mathbb{K} .

structures, global Galerkin techniques analogous to those in Section 8.2 can be more efficient to implement for beam discretization. The global discretization also demonstrates similarities and differences between the interpolatory cubic Hermite approximates and the projective cubic spline technique discussed in Section 8.3.1.

For the partition $x_j = jh$, $h = \frac{\ell}{N}$, $j = 0, \dots, N$, the global Hermite basis functions are taken to be

$$\phi_{w_j}(x) = \frac{1}{h^3} \begin{cases} (x - x_{j-1})^2[2(x_j - x) + h] & , \quad x \in [x_{j-1}, x_j] \\ (x_{j+1} - x)^2[2(x - x_j) + h] & , \quad x \in (x_j, x_{j+1}] \\ 0 & , \quad \text{otherwise} \end{cases}$$

$$\phi_{\theta_j}(x) = \frac{1}{h^2} \begin{cases} (x - x_{j-1})^2(x - x_j) & , \quad x \in [x_{j-1}, x_j] \\ (x_{j+1} - x)^2(x - x_j) & , \quad x \in (x_j, x_{j+1}] \\ 0 & , \quad \text{otherwise} \end{cases}$$

for $j = 1, \dots, N - 1$. The definitions of ϕ_{w_N} and ϕ_{θ_N} are analogous but involves only the interval $[x_{N-1}, x_N]$. As illustrated in Figure 8.16, the global basis functions ϕ_{w_j} and ϕ_{θ_j} are the concatenation of the local displacement elements $\tilde{\phi}_3, \tilde{\phi}_1$ and slope elements $\tilde{\phi}_4, \tilde{\phi}_2$ defined in (8.34) and shown in Figure 8.12.

The approximating subspace is taken to be

$$V^N = \text{span} \{ \phi_{w_j}, \phi_{\theta_j} \}_{j=1}^N$$

and the approximate solution is

$$w^N(t, x) = \sum_{j=1}^N w_j(t) \phi_{w_j}(x) + \sum_{j=1}^N \theta_j(t) \phi_{\theta_j}(x). \tag{8.36}$$

We note that by omitting ϕ_{w_0} and ϕ_{θ_0} , elements $v \in V^N$ are guaranteed to satisfy $v(0) = v'(0) = 0$ which ensures that $V^N \subset V = H_0^2(0, \ell)$. The ordering of nodal coefficients provided by (8.36) yields banded, tridiagonal mass, damping and stiffness matrices that are Toeplitz along all but the last row and column.

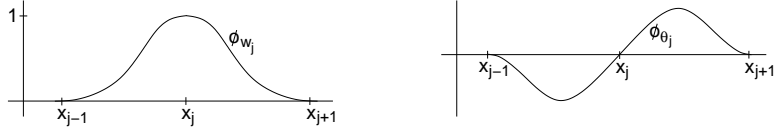


Figure 8.16. Global Hermite basis functions ϕ_{w_j} and ϕ_{θ_j} .

The projection of (8.26) onto V^N and use of basis functions as test functions yields the second-order system

$$\mathbb{M}\ddot{\mathbf{w}} + \mathbb{Q}\dot{\mathbf{w}} + \mathbb{K}\mathbf{w} = \mathbf{f} + V(t)\mathbf{b}$$

where the $2N \times 1$ vector $\mathbf{w}(t)$ has the nodal ordering

$$\mathbf{w}(t) = [w_1(t), \dots, w_N(t), \theta_1(t), \dots, \theta_N(t)]^T.$$

The global system matrices $\mathbb{M}, \mathbb{Q}, \mathbb{K}$ and vectors \mathbf{f}, \mathbf{b} have definitions analogous to (8.31) and (8.32) where ϕ_i and ϕ_j now represent the combined basis $\{\phi_{w_i}, \phi_{\theta_i}\}$ and $\{\phi_{w_j}, \phi_{\theta_j}\}$. As with the matrices arising from the cubic B-spline discretization discussed in Section 8.3.1, the integrals involve piecewise polynomials of degree less than or equal to 6 so exact integration is achieved using the composite 4-point Gauss–Legendre rule (8.12) on each subinterval $[x_{j-1}, x_j]$.

For constant stiffness YI , this yields the stiffness matrix

$$\mathbb{K} = \frac{YI}{h^3} \begin{bmatrix} 24 & -12 & & & 0 & 6h \\ -12 & 24 & -12 & & -6h & 0 & 6h \\ & \ddots & \ddots & \ddots & & \ddots & \ddots & \ddots \\ & & -12 & 24 & -12 & & -6h & 0 & 6h \\ & & & 12 & 12 & & & -6h & -6h \\ \hline 0 & -6h & & & 8h^2 & 2h^2 & & & \\ 6h & 0 & -6h & & 2h^2 & 8h^2 & 2h^2 & & \\ & \ddots & \ddots & \ddots & & \ddots & \ddots & \ddots & \\ & & 6h & 0 & -6h & & 2h^2 & 8h^2 & 2h^2 \\ & & & 6h & -6h & & 2h^2 & 4h^2 & \end{bmatrix}. \quad (8.37)$$

It is observed that the stiffness matrix \mathbb{K} in (8.35), which was derived through elemental analysis, is a special case of (8.37) when $N = 2$. For the beam with surface-mounted patches, the differing values of YI in the patch region are simply incorporated in those regions of the partition which coincide with the patch. The mass and damping matrices are constructed in an analogous manner.

We note that the parameter ordering $\mathbf{w}(t) = [w_1(t), \theta_1(t), \dots, w_N(t), \theta_N(t)]^T$ eliminates the block tridiagonal structure and yields block diagonal matrices where

each block has a support of 6 diagonals. The disadvantage of this ordering scheme is that the Toeplitz nature of the matrices is destroyed which complicates matrix construction. Additional details regarding elemental and global approximation using cubic Hermite elements can be found in [36, 203, 422].

8.3.3 Comparison between Cubic Spline and Cubic Hermite Approximates

The cubic B-spline and cubic Hermite techniques detailed in Sections 8.3.1 and 8.3.2 illustrate two commonly employed Galerkin techniques for approximating beam models. Both provide $\mathcal{O}(h^4)$ spatial convergence rates as long as partitions are aligned with patches to accommodate discontinuities in mass, damping, stiffness and input parameters. As noted in Section 8.3.1, the cubic spline discretization is a projection method whereas the cubic Hermite method is interpolatory in the sense that the coefficients $\mathbf{w}(t)$ are nodal values of the displacement and slope at the partition points. Hence the cubic spline technique is more closely related to general Galerkin expansions — e.g., employing Legendre or Fourier bases — whereas the cubic Hermite expansion employs the finite element philosophy which, as detailed on pages 417–419 of Appendix A, is subsumed in the Galerkin framework.

The primary advantage of the cubic Hermite method lies in its interpolatory nature. This simplifies the enforcement of essential boundary conditions and facilitates characterization of complex structures which require nodal matching at the junction of differing geometries. For example, the transition from flat tabs to the curved patch region in THUNDER transducers — see the models (7.103), (7.106), or (7.107) in Section 7.9 — is easily accommodated by matching nodal values with Hermite elements whereas it is difficult to implement with cubic splines.

The disadvantage of the Hermite approximate is that it requires roughly twice as many coefficients as the spline expansion since both displacements and slopes are discretized. The increased dimensionality of system matrices must be accommodated when employing the model for control designs which require real-time implementation.

8.3.4 Examples and Software

Attributes of the discretized beam model, when used to characterize the PVDF–polyimide unimorph depicted in Figure 7.13, are illustrated in Section 7.4.1. Experimental validation of the discretized model for a beam with surface-mounted piezoceramic patches is addressed in Chapter 5 of [33].

MATLAB m-files for implementing the unimorph and beam models are located at the website <http://www.siam.org/books/fr32>.

8.4 Numerical Approximation of the Plate Model

In this section, we summarize approximation techniques for the rectangular and circular plate models developed in Section 7.5. We consider regimes in which transverse and longitudinal displacements can be decoupled and focus on approximating

the former using Galerkin expansions employing spline or Fourier bases in space. As illustrated in Section 8.5 when discussing thin shell approximation, linear elements can be employed to discretize longitudinal displacements if warranted by the application. A full discussion regarding finite element methods for plates is beyond the scope of this discussion and the reader is referred to [276, 390, 422, 527] for details about this topic.

8.4.1 Rectangular Plate Approximation

We consider a rectangular plate with $x \in [0, \ell]$ and $y \in [0, a]$ as depicted in Figure 7.17. As in Section 7.5.1, we assume that the plate has thickness h and has N_A surface-mounted piezoceramic patches of thickness h_I whose edges are parallel with the x and y -axes. The plate is assumed to have fixed-edge conditions at $x = 0$, $y = 0$ and free boundary conditions for the remaining two edges. To simplify notation, we let $\Omega = [0, \ell] \times [0, a]$ denote the plate region. Finally, we consider linear input regimes with voltages $V_i(t) = V_{1i}(t) = -V_{2i}(t)$. Extension to nonlinear input regimes follows immediately when voltage inputs are replaced by the nonlinear polarization relations.

From (7.65), the transverse displacements are quantified by the weak model formulation

$$\int_{\Omega} \left\{ \rho \frac{\partial^2 w}{\partial t^2} \phi - M_x \frac{\partial^2 \phi}{\partial x^2} - 2M_{xy} \frac{\partial^2 \phi}{\partial x \partial y} - M_y \frac{\partial^2 \phi}{\partial y^2} - f_n \phi \right\} d\omega = 0 \quad (8.38)$$

for ϕ in the space of test functions

$$V = H_0^2(\Omega) = \{ \phi \in H^2(\Omega) \mid \phi(0, y) = \phi_x(0, y) = 0 \text{ for } 0 \leq y \leq a, \\ \phi(x, 0) = \phi_y(x, 0) = 0 \text{ for } 0 \leq x \leq \ell \}.$$

The density ρ is specified by (7.48) and the moments are defined in (7.57) with components specified in (7.58)–(7.63). We consider the case of linear patch inputs but note that nonlinear inputs are accommodated in an identical manner.

The philosophy when approximating the dynamics of (8.38) is identical to that employed in Sections 8.2 and 8.3 for the rod and beam models. The relation is projected onto a spline-based finite-dimensional subspace $V^N \subset V$ to obtain a semi-discrete system appropriate for finite-dimensional control design. This vector-valued system can subsequently be simulated by employing finite difference discretizations in time or standard software for moderately stiff systems.

Consider a partition $\{(x_m, y_n)\}$ of Ω where $x_m = mh_x$, $y_n = nh_y$, with $h_x = \frac{\ell}{N_x}$, $h_y = \frac{a}{N_y}$ and $m = 0, \dots, N_x$, $n = 0, \dots, N_y$. Using the definition (8.28), we define modified cubic spline basis functions $\phi_m(x)$ and $\phi_n(y)$ on the intervals $[0, \ell]$ and $[0, a]$. The product space basis is then taken to be

$$\Phi_k(x, y) = \phi_m(x)\phi_n(y) \quad (8.39)$$

and the approximating subspace is

$$V^N = \text{span} \{ \Phi_k \}_{k=1}^{N_w}$$

where $N_w = (N_x + 1)(N_y + 1)$. Approximate displacements have the representation

$$\begin{aligned} w^N(t, x, y) &= \sum_{k=1}^{N_w} w_k(t) \Phi_k(x, y) \\ &= \sum_{m=1}^{N_x+1} \sum_{n=1}^{N_y+1} w_{mn}(t) \phi_m(x) \phi_n(y). \end{aligned}$$

The restriction of the infinite-dimensional model (8.38) to the finite-dimensional subspace $V^N \subset V$ yields the vector-valued system

$$\mathbb{M} \ddot{\mathbf{w}} + \mathbb{Q} \dot{\mathbf{w}} + \mathbb{K} \mathbf{w} = \mathbf{f} + \frac{2Y_A d_{31} c_2}{h_A (1 - \nu_A)} \sum_{i=1}^{N_A} V_i(t) \mathbf{b}_i \quad (8.40)$$

where $\mathbf{w}(t) = [w_1(t), \dots, w_{N_w}(t)]^T$. The mass and stiffness matrices are defined componentwise by

$$\begin{aligned} [\mathbb{M}]_{jk} &= \int_{\Omega} \rho \Phi_j \Phi_k d\omega \\ [\mathbb{K}]_{jk} &= [\mathbb{K}_1]_{jk} + [\mathbb{K}_2]_{jk} + [\mathbb{K}_3]_{jk} + [\mathbb{K}_4]_{jk} + [\mathbb{K}_5]_{jk} \end{aligned}$$

where

$$\begin{aligned} [\mathbb{K}_1]_{jk} &= \int_{\Omega} \left(\frac{Y_I h_I^3}{12(1 - \nu_I^2)} + \frac{2Y_A c_3}{1 - \nu_A^2} \sum_{i=1}^{N_A} \chi_{pe_i}(x, y) \right) \frac{\partial^2 \Phi_j}{\partial x^2} \frac{\partial^2 \Phi_k}{\partial x^2} d\omega \\ [\mathbb{K}_2]_{jk} &= \int_{\Omega} \left(\frac{Y_I h_I^3 \nu_I}{12(1 - \nu_I^2)} + \frac{2Y_A c_3 \nu_A}{1 - \nu_A^2} \sum_{i=1}^{N_A} \chi_{pe_i}(x, y) \right) \frac{\partial^2 \Phi_j}{\partial x^2} \frac{\partial^2 \Phi_k}{\partial y^2} d\omega \\ [\mathbb{K}_3]_{jk} &= \int_{\Omega} \left(\frac{Y_I h_I^3}{12(1 - \nu_I^2)} + \frac{2Y_A c_3}{1 - \nu_A^2} \sum_{i=1}^{N_A} \chi_{pe_i}(x, y) \right) \frac{\partial^2 \Phi_j}{\partial y^2} \frac{\partial^2 \Phi_k}{\partial y^2} d\omega \\ [\mathbb{K}_4]_{jk} &= \int_{\Omega} \left(\frac{Y_I h_I^3 \nu_I}{12(1 - \nu_I^2)} + \frac{2Y_A c_3 \nu_A}{1 - \nu_A^2} \sum_{i=1}^{N_A} \chi_{pe_i}(x, y) \right) \frac{\partial^2 \Phi_j}{\partial y^2} \frac{\partial^2 \Phi_k}{\partial x^2} d\omega \\ [\mathbb{K}_5]_{jk} &= \int_{\Omega} \left(\frac{Y_I h_I^3}{12(1 + \nu_I)} + \frac{Y_A c_3}{1 + \nu_A} \sum_{i=1}^{N_A} \chi_{pe_i}(x, y) \right) \frac{\partial^2 \Phi_j}{\partial x \partial y} \frac{\partial^2 \Phi_k}{\partial x \partial y} d\omega. \end{aligned}$$

The damping matrix \mathbb{Q} is constructed in a manner analogous to \mathbb{K} . Finally, the vectors are defined by

$$\begin{aligned} [\mathbf{f}]_j &= \int_{\Omega} f_n \Phi_j d\omega \\ [\mathbf{b}_i]_j &= \int_{\Omega} \chi_{pe_i}(x, y) \left(\frac{\partial^2 \Phi_j}{\partial x^2} + \frac{\partial^2 \Phi_j}{\partial y^2} \right) d\omega. \end{aligned}$$

The second-order system (8.40) has the same form as (8.16) which was developed for the rod in Section 8.2.1. Hence the techniques in that section can be used to construct a corresponding first-order system appropriate for control design or simulation.

8.4.2 Circular Plate Approximation

The circular plate model (7.71) with space of test functions (7.70) represents a setting in which the geometry and differential operator are not the tensor product of 1-D components. When combined with the inherent periodicity in θ , this motivates consideration of basis elements comprised of cubic B-splines in r and Fourier components in θ . We provide here an outline of the approximate system construction and refer the reader to [430] for details regarding this development.

The circumferential component of the basis is taken to be $\phi_m(\theta) = e^{im\theta}$ where $m = -M, \dots, M$. The form of the radial component is motivated by the analytic Bessel behavior of the undamped plate that is devoid of patches. Let $\phi_n^m(r)$ denote the n th cubic spline modified to satisfy $\phi_n^m(a) = \frac{d\phi_n^m(a)}{dr} = 0$ — e.g., see (8.28) — along with the condition $\frac{d\phi_n^m(0)}{dr} = 0$ which is required to ensure differentiability at the origin.

The plate basis is then taken to be

$$\Phi_k(r, \theta) = r^{|\hat{m}|} \phi_n^m(r) e^{im\theta}$$

where

$$\hat{m} = \begin{cases} 0 & , \quad m = 0 \\ 1 & , \quad m \neq 0. \end{cases}$$

As detailed in [430], the inclusion of the weighting term $r^{|\hat{m}|}$ is motivated by the asymptotic behavior of the Bessel functions as $r \rightarrow 0$ and ensures the uniqueness of the solution at the origin. The approximating subspace is

$$V^N = \text{span}\{\Phi_k\}$$

and approximate solutions have the representation

$$\begin{aligned} w^N(t, r, \theta) &= \sum_{k=1}^{N_w} w_k(t) \Phi_k(r, \theta) \\ &= \sum_{m=-M}^M \sum_{n=1}^{N^m} w_{mn}(t) r^{|\hat{m}|} \phi_n^m(r) e^{im\theta}. \end{aligned}$$

Here

$$N^m = \begin{cases} N & , \quad m = 0 \\ N + 1 & , \quad m \neq 0. \end{cases}$$

where N denotes the number of modified cubic splines.

Details regarding the construction of component matrices and vectors are provided in [430]. The performance of the discretized model when characterizing the dynamics of a circular plate is summarized in Section 7.5 and detailed in [430].

8.4.3 Examples and Software

The accuracy and limitations of the discretized circular plate model for characterizing both axisymmetric and nonaxisymmetric plate vibrations are illustrated in Section 7.5.2. In the axisymmetric case, the model accurately quantifies low to moderate frequency dynamics but overdamps high frequency modes which is characteristic of the Kelvin–Voigt damping model. It is illustrated that in the non-axisymmetric regime, which is truly 2-D, the model accurately characterizes the dynamics associated with 8 of the 11 measured modes.

The reader can obtain MATLAB m-files for the approximation of the rectangular plate model at the website <http://www.siam.org/books/fr32>.

8.5 Numerical Approximation of the Shell Model

The final structure under consideration is the cylindrical shell model (7.92) developed in Section 7.7. To simplify the discussion, we consider fixed-edge conditions $u = v = w = \frac{\partial w}{\partial x} = 0$ at $x = 0, \ell$ and hence the space of test functions is

$$V = H_0^1(\Omega) \times H_0^1(\Omega) \times H_0^2(\Omega)$$

where $\Omega = [0, \ell] \times [0, 2\pi]$ denotes the shell region and

$$H_0^1(\Omega) = \{\phi \in H^1(\Omega) \mid \phi(0, \theta) = \phi(\ell, \theta) = 0\}$$

$$H_0^2(\Omega) = \{\phi \in H^2(\Omega) \mid \phi(0, \theta) = \phi(\ell, \theta) = \phi_x(0, \theta) = \phi_x(\ell, \theta) = 0\}.$$

We summarize here the cubic spline–Fourier approximation method developed in [130] and illustrated for control design in [131]. As noted in the first citation, two phenomena which plague the approximation of shell models are *shear locking* and *membrane* or *shear-membrane locking*. Shear locking, which has also been studied extensively in the context of Reissner–Mindlin plate models, is due to element incompatibility when enforcing the Kirchhoff–Love constraint of vanishing transverse shear strains as the shell thickness h tends to zero [14]. Membrane locking occurs when the total deformation energy is bending-dominated and is due to smoothness and asymptotic constraints in the shell model which are not appropriately represented by the approximation method — e.g., [21, 22, 290, 380]. If these constraints are not satisfied by approximating elements, the numerical solution is often overly stiff in the sense that the model exhibits bending dynamics which the approximate solution cannot match. As detailed in [290], mesh sizes must be chosen significantly smaller than the shell thickness to ensure accurate approximations with high-order finite elements in such bending-dominated regimes. It is noted that even with such mesh size restrictions, low-order finite element methods often fail in such regimes.

The discussion in this section is meant to provide the reader with an overview of issues associated with shell approximation and a brief summary of one discretization technique. Details and subtleties associated with this topic can found in [39, 192] and previously cited references.

Basis Construction and Approximating Subspaces

To approximate the longitudinal, circumferential and transverse displacements u, v and w , it is necessary to construct bases for finite-dimensional subspaces of $H_0^1(\Omega)$ and $H_0^2(\Omega)$. This is accomplished using linear and cubic splines modified to accommodate the fixed boundary conditions.

We consider a uniform partition along the x -axis with gridpoints $x_n = nh$, $h = \frac{\ell}{N}$ and $n = 0, \dots, N$. For $n = 1, \dots, N - 1$, we employ the linear splines

$$\phi_{u_n}(x) = \phi_{v_n}(x) = \frac{1}{h} \begin{cases} x - x_{n-1}, & x_{n-1} \leq x < x_n \\ x_{n+1} - x, & x_n \leq x \leq x_{n+1} \\ 0, & \text{otherwise} \end{cases}$$

and modified cubic splines

$$\widehat{\phi}_{w_n}(x) = \begin{cases} \widehat{\phi}_0(x) - 2\widehat{\phi}_{-1}(x) - 2\widehat{\phi}_1(x), & n = 1 \\ \widehat{\phi}_n(x), & n = 2, \dots, N - 2 \\ \widehat{\phi}_N(x) - 2\widehat{\phi}_{N-1}(x) - 2\widehat{\phi}_{N+1}(x), & n = N - 1 \end{cases}$$

where the standard B-splines are defined in (8.27). For $n = 1, \dots, N - 1$ and $m = -M, \dots, M$, the product space bases, in complex form, are taken to be

$$\begin{aligned} \Phi_{u_k}(\theta, x) &= e^{im\theta} \phi_{u_n}(x) \\ \Phi_{v_k}(\theta, x) &= e^{im\theta} \phi_{v_n}(x) \\ \Phi_{w_k}(\theta, x) &= e^{im\theta} \widehat{\phi}_{w_n}(x). \end{aligned}$$

To provide an equivalent real form, one can employ the representation

$$\Phi_{u_k}(\theta, x) = \begin{Bmatrix} \cos(m\theta) \\ 1 \\ \sin(m\theta) \end{Bmatrix} \phi_{u_n}(x), \quad m = 1, \dots, M$$

with similar definitions for Φ_{v_k} and Φ_{w_k} . The approximating subspaces are

$$\begin{aligned} V_u^N &= \text{span} \{ \Phi_{u_k} \}_{k=1}^{N_u} \\ V_v^N &= \text{span} \{ \Phi_{v_k} \}_{k=1}^{N_v} \\ V_w^N &= \text{span} \{ \Phi_{w_k} \}_{k=1}^{N_w} \end{aligned}$$

and the approximate displacements are represented by the expansions

$$\begin{aligned} u^N(t, \theta, x) &= \sum_{k=1}^{N_u} u_k(t) \Phi_{u_k}(\theta, x) \\ v^N(t, \theta, x) &= \sum_{k=1}^{N_v} v_k(t) \Phi_{v_k}(\theta, x) \\ w^N(t, \theta, x) &= \sum_{k=1}^{N_w} w_k(t) \Phi_{w_k}(\theta, x). \end{aligned} \tag{8.41}$$

For a single partition, it follows that $N_u = N_v = N_w = (2N - 1)(2M + 1)$. Through the construction of ϕ_{u_n}, ϕ_{v_n} and ϕ_{w_n} , the approximate displacements u^N, v^N and w^N satisfy the fixed-end conditions and $V^N = V_u^N \times V_v^N \times V_w^N \subset V$. We note that consideration of real components yields the equivalent representation

$$u^N(t, \theta, x) = \sum_{n=1}^{N-1} u_{0n}(t) \phi_{u_n}(x) + \sum_{m=1}^M \sum_{n=1}^{N-1} u_{mn}(t) \cos(m\theta) \phi_{u_n}(x) + \sum_{m=1}^M \sum_{n=1}^{N-1} \tilde{u}_{mn}(t) \sin(m\theta) \phi_{u_n}(x)$$

with similar expressions for $v^N(t, \theta, x)$ and $w^N(t, \theta, x)$.

System Matrices

To determine the generalized Fourier coefficients $u_k(t), v_k(t)$ and $w_k(t)$, we employ the same approach as in previous sections and orthogonalize the residual with respect to the linearly independent test functions used to construct the approximating subspaces. To construct the resulting vector-valued system, we consolidate the coefficients in the vectors

$$\mathbf{u}(t) = \begin{bmatrix} u_1(t) \\ \vdots \\ u_{N_u}(t) \end{bmatrix}, \quad \mathbf{v}(t) = \begin{bmatrix} v_1(t) \\ \vdots \\ v_{N_v}(t) \end{bmatrix}, \quad \mathbf{w}(t) = \begin{bmatrix} w_1(t) \\ \vdots \\ w_{N_w}(t) \end{bmatrix}.$$

The full set of coefficients is then represented as $\boldsymbol{\vartheta}(t) = [\mathbf{u}(t), \mathbf{v}(t), \mathbf{w}(t)]^T$ where $N = N_u + N_v + N_w$.

The mass, stiffness and damping matrices have the form

$$\mathbb{M} = \begin{bmatrix} \mathbb{U}_m & & \\ & \mathbb{V}_m & \\ & & \mathbb{W}_m \end{bmatrix},$$

$$\mathbb{K} = \begin{bmatrix} \mathbb{U}_{11} + \mathbb{U}_{12} & \mathbb{V}_{11} + \mathbb{V}_{12} & \mathbb{W}_{11} \\ \mathbb{U}_{21} + \mathbb{U}_{22} & \mathbb{V}_{21} + \mathbb{V}_{22} & \mathbb{W}_{21} \\ \mathbb{U}_{31} & \mathbb{V}_{31} & \sum_{k=1}^6 \mathbb{W}_{3k} \end{bmatrix},$$

$$\mathbb{Q} = \begin{bmatrix} \tilde{\mathbb{U}}_{11} + \tilde{\mathbb{U}}_{12} & \tilde{\mathbb{V}}_{11} + \tilde{\mathbb{V}}_{12} & \tilde{\mathbb{W}}_{11} \\ \tilde{\mathbb{U}}_{21} + \tilde{\mathbb{U}}_{22} & \tilde{\mathbb{V}}_{21} + \tilde{\mathbb{V}}_{22} & \tilde{\mathbb{W}}_{21} \\ \tilde{\mathbb{U}}_{31} & \tilde{\mathbb{V}}_{31} & \sum_{k=1}^6 \tilde{\mathbb{W}}_{3k} \end{bmatrix}$$

and the exogenous vectors are

$$\mathbf{f}(t) = [\mathbf{f}_u, \mathbf{f}_v, \mathbf{f}_w]^T, \quad \mathbf{b} = [\mathbf{b}_u, \mathbf{b}_v, \mathbf{0}]^T.$$

The various submatrices contain individual components which arise when the weak formulation (7.92) is restricted to V^N . For example, the approximation of the mass and stiffness components in the longitudinal equation of (7.92) yields

$$\begin{aligned}
 [\mathbb{U}_m]_{jk} &= \int_{\Omega} \rho h R \Phi_{u_k} \Phi_{u_j} d\omega, \\
 [\mathbb{U}_{11}]_{jk} &= \int_{\Omega} \frac{Y h R}{1 - \nu^2} \frac{\partial \Phi_{u_k}}{\partial x} \frac{\partial \Phi_{u_j}}{\partial x} d\omega, \\
 [\mathbb{V}_{11}]_{jk} &= \int_{\Omega} \frac{Y h \nu}{1 - \nu^2} \frac{\partial \Phi_{u_k}}{\partial \theta} \frac{\partial \Phi_{u_j}}{\partial x} d\omega, \\
 [\mathbb{W}_{11}]_{jk} &= \int_{\Omega} \frac{Y h \nu}{1 - \nu^2} \Phi_{w_k} \frac{\partial \Phi_{u_j}}{\partial x} d\omega, \\
 [\mathbb{V}_{12}]_{jk} &= \int_{\Omega} \frac{Y h}{2(1 + \nu)} \frac{\partial \Phi_{u_k}}{\partial x} \frac{\partial \Phi_{u_j}}{\partial \theta} d\omega, \\
 [\mathbb{U}_{12}]_{jk} &= \int_{\Omega} \frac{Y h}{2R(1 + \nu)} \frac{\partial \Phi_{u_k}}{\partial \theta} \frac{\partial \Phi_{u_j}}{\partial \theta} d\omega, \\
 [\mathbf{f}_u]_j &= \int_{\Omega} R f_x \Phi_{u_j} d\omega, \\
 [\mathbf{b}_u]_j &= \int_{\Omega} \frac{R h}{1 - \nu} \frac{\partial \Phi_{u_j}}{\partial x} d\omega
 \end{aligned}$$

with similar expressions for the remaining submatrices.

In the usual manner, the second-order system

$$\begin{aligned}
 \mathbb{M} \ddot{\boldsymbol{\vartheta}}(t) + \mathbb{Q} \dot{\boldsymbol{\vartheta}}(t) + \mathbb{K} \boldsymbol{\vartheta}(t) &= \mathbf{f}(t) + [a_1(P(E(t)) - P_R) + a_2(P(E(t)) - P_R)^2] \mathbf{b} \\
 \boldsymbol{\vartheta}(0) = \vartheta_0, \quad \dot{\boldsymbol{\vartheta}}(0) &= \vartheta_1
 \end{aligned}$$

can be reformulated as the first-order Cauchy equation

$$\begin{aligned}
 \dot{\mathbf{z}}^N(t) &= \mathbb{A} \mathbf{z}(t) + \mathbf{F}(t) + [a_1(P(E(t)) - P_R) + a_2(P(E(t)) - P_R)^2] \mathbf{B} \\
 \mathbf{z}(0) &= \mathbf{z}_0,
 \end{aligned}$$

where $\mathbf{z} = [\boldsymbol{\vartheta}(t), \dot{\boldsymbol{\vartheta}}(t)]^T$ and

$$\mathbb{A} = \begin{bmatrix} 0 & \mathbb{I} \\ -\mathbb{M}^{-1} \mathbb{K} & -\mathbb{M}^{-1} \mathbb{Q} \end{bmatrix}, \quad \mathbf{F}(t) = \begin{bmatrix} 0 \\ \mathbb{M}^{-1}(\mathbf{f}(t)) \end{bmatrix}, \quad \mathbf{B} = \begin{bmatrix} 0 \\ \mathbb{M}^{-1} \mathbf{b} \end{bmatrix}.$$

The system in this form is amenable to simulation, parameter estimation and control design. Note that the system can be adapted to alternative boundary conditions through modifications of the first and last basis functions. Flexibility in this regard is also a hallmark of the method.